Martin, A.C.H.; Boutin, J.; Hauser, D.; Dinnat, E. P.. 2014 Active-passive synergy for interpreting ocean L-band emissivity: Results from the CAROLS airborne campaigns. *Journal of Geophysical Research: Oceans*, 119 (8). 4940-4957. 10.1002/2014JC009890

Martin, A.C.H.; Boutin, J.; Hauser, D.; Dinnat, E. P.. 2014 Active-passive synergy for interpreting ocean L-band emissivity: Results from the CAROLS airborne campaigns. *Journal of Geophysical Research: Oceans*, 119 (8). 4940-4957. 10.1002/2014JC009890

AGU PUBLICATIONS

JGR

Journal of Geophysical Research: Oceans

RESEARCH ARTICLE
10.1002/2014JC009890

Special Section:
Early scientific results from the salinity measuring satellites Aquarius/SAC-D and SMOS

Active-passive synergy for interpreting ocean L-band emissivity: Results from the CAROLS airborne campaigns

A. C. H. Martin[1,2], J. Boutin[1], D. Hauser[3], and E. P. Dinnat[4,5]

[1]Sorbonne Universités, UPMC Univ Paris 6, CNRS, IRD, MNHN, LOCEAN-IPSL, Paris, France, [2]National Oceanography Centre, Marine Physics and Ocean Climate, Southampton, UK, [3]Université de Versailles St-Quentin, Sorbonne Universités, UPMC Univ Paris 6, CNRS, LATMOS-IPSL, Guyancourt, France, [4]Center of Excellence in Earth Systems Modeling & Observations, Chapman University, Orange, California, USA, [5]NASA Goddard Space Flight Center, Cryospheric Sciences Laboratory, Greenbelt, Maryland, USA

Abstract The impact of the ocean surface roughness on the ocean L-band emissivity is investigated using simultaneous airborne measurements from an L-band radiometer (CAROLS) and from a C-band scatterometer (STORM) acquired in the Gulf of Biscay (off-the French Atlantic coasts) in November 2010. Two synergetic approaches are used to investigate the impact of surface roughness on the L-band brightness temperature (Tb). First, wind derived from the scatterometer measurements is used to analyze the roughness contribution to Tb as a function of wind and compare it with the one simulated by SMOS and Aquarius roughness models. Then residuals from this mean relationship are analyzed in terms of mean square slope derived from the STORM instrument. We show improvement of new radiometric roughness models derived from SMOS and Aquarius satellite measurements in comparison with prelaunch models. Influence of wind azimuth on Tb could not be evidenced from our data set. However, we point out the importance of taking into account large roughness scales (>20 cm) in addition to small roughness scale (5 cm) rapidly affected by wind to interpret radiometric measurements far from nadir. This was made possible thanks to simultaneous estimates of large and small roughness scales using STORM at small (7–16°) and large (30°) incidence angles.

Key Points:
- Confirm new L-band radiometric roughness models improvement
- H-pol Tb double dependence on both wind speed and filtered mss
- Wind azimuth influence on CAROLS Ta lower than 0.2 K (wind speed >12 m/s)

Correspondence to:
A. C. H. Martin,
admartin@noc.ac.uk

Citation:
Martin, A. C. H., J. Boutin, D. Hauser, and E. P. Dinnat (2014), Active-passive synergy for interpreting ocean L-band emissivity: Results from the CAROLS airborne campaigns, *J. Geophys. Res. Oceans*, *119*, 4940–4957, doi:10.1002/2014JC009890.

Received 4 FEB 2014
Accepted 6 JUL 2014
Accepted article online 11 JUL 2014
Published online 11 AUG 2014

1. Introduction

Remote sensing of sea surface salinity (SSS) is very challenging because the signal-to-noise ratio is very small and because the influence of SSS on the L-band radiometric signal is of the same order as one of the other geophysical parameters, in particular sea surface roughness [*Dinnat et al.*, 2003; *Yueh et al.*, 2010]. The first two satellite missions carrying a L-band radiometer, Soil Moisture and Ocean Salinity (SMOS) launched in 2009 and Aquarius launched in 2011, already give very interesting results [e.g., *Font et al.*, 2012; *Lagerloef et al.*, 2012; *Lee et al.*, 2012; *Alory et al.*, 2012; *Reul et al.*, 2013] but mainly for signals with high contrast in SSS (>0.5 pss)—we used the Practical Salinity Scale (pss-78) as recommended in *IOC et al.* [2010] as remote sensing measurements rely on sea conductivity, that we simplify for convenience here as pss. To achieve the objective of 0.1–0.2 pss over spatiotemporal scales of 100 × 100 km^2 to 200 × 200 km^2 and 10–30 days, the impact of sea surface roughness has to be corrected with a good accuracy.

In the 1970s, several experiments studied wind (sea roughness and foam) and SSS influence on L-band brightness temperature (Tb), evidencing the technical difficulty for building a satellite instrument with sufficiently low radiometric noise to provide useful information to the scientific community. A renewal of interest occurred at the end of the 1990s with technology improvements [*Lagerloef et al.*, 1995] that lead to the preparation of the two satellite missions. Measurements on platform or tower [*Camps et al.*, 2004; *Gabarró et al.*, 2004], as well as airborne measurements [*Etcheto et al.*, 2004; *Reul et al.*, 2008], permitted to sample various and well-documented geophysical conditions and to validate the SMOS prelaunch roughness models at the first order. But these measurements were acquired in regions relatively close to coasts, in enclosed sea so that one may expect local conditions to be different from the ones over open ocean. Using simultaneous airborne radar measurements of wind speed and radiometric L-band signal further from the coast, *Yueh et al.* [2010] showed an upwind-crosswind signature for wind speed at 14 and 24 m/s and derived the Tb sensitivity to wind speed for incidence angles up to 80°.

Based on new SMOS and Aquarius satellite data, new roughness models have been proposed. *Guimbard et al.* [2012] and N. Reul and J. Tenerelli (personal communication, 2012) proposed new empirical roughness

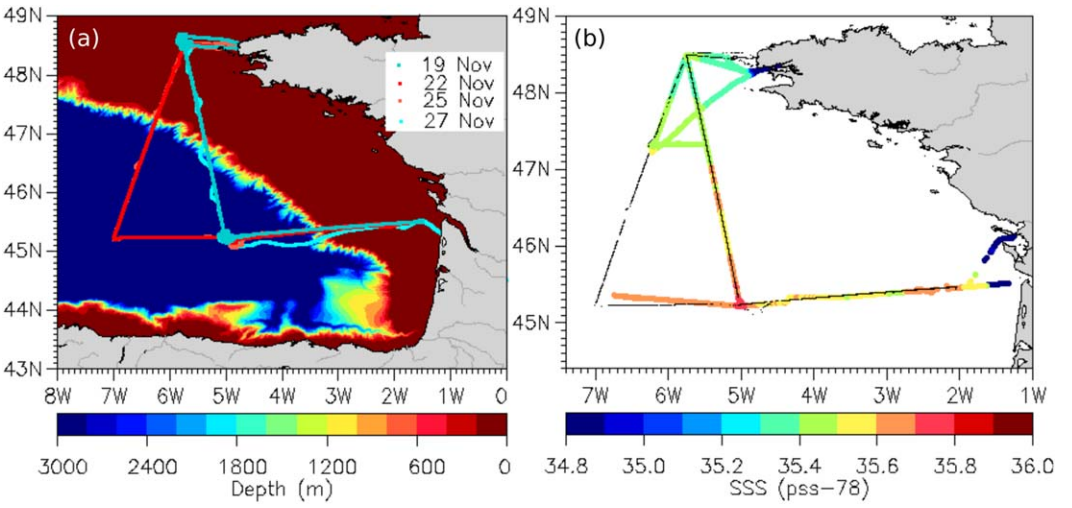

Figure 1. (a) Flight track superimposed on a bathymetry base map. In two tones of blue for morning flights (19th and 27th), in red and orange for evening flights (22th and 25th). (b) Sea surface salinity measured along the main part of flight tracks by the RV CDLM.

models using SMOS data as function of only wind speed (no wind direction dependency). *Yin et al*. [2012] adjust a physical model on the SMOS data. The resulting model is a function mostly dependent on wind speed, and on wind direction to a lesser extent. However, it has not been possible to evidence a wind direction dependency from SMOS data, likely because of their large noise. Using Aquarius L-band measurements, which have a better instantaneous radiometric accuracy than SMOS, *Yueh et al*. [2013] proposed a new roughness model function of wind speed and wind direction. Despite these new roughness models, SMOS SSS accuracy [on the order of 0.15–0.3 pss in the tropics and subtropics, *Boutin et al*., 2013; *Hernandez et al*., 2014] is not as good as expected if one considers only the radiometric noise as uncertainty source [*Boutin et al*., 2004]. It is suspected that inaccuracies in forward models may be one significant source of uncertainty.

The aim of this study is to assess the improvements of the new satellite roughness models, to understand their weaknesses, and to investigate part of signals not explained by forward models presently used for SMOS or Aquarius. Data used have been acquired during the CAROLS (Combined Airborne Radio-instruments for Ocean and Land Studies) campaign of November 2010 using a high accuracy L-band radiometer (called CAROLS for Cooperative Airborne Radiometer for Ocean and Land Studies) and a C-band scatterometer (called STORM for Système de Télédétection pour l'Observation de la Mer).

In section 2, we describe the airborne campaign as well as the radiometric and radar data. Section 3 presents the models of antenna temperature (T_A) excess induced by sea surface roughness after integration on the CAROLS antenna pattern. Section 4 presents the results using the synergy between CAROLS and STORM. These results are discussed in section 5 and key results are summarized in section 6.

2. Campaign and Data Description

2.1. CAROLS Campaign

The CAROLS campaigns were performed from 2007 to 2010 over the ocean in the Bay of Biscay off the coast of France and Spain. In this paper, we concentrate on the last series of campaigns in November 2010 because it offered the most variable geophysical conditions. The CAROLS L-band radiometer and the STORM C-band scatterometer were installed on the French research airplane ATR42. The campaign's aim was to study the impact of sea surface roughness on radiometric signal. Four flights were carried out at an altitude of about 2000 or 3000 m above the sea surface at an airspeed of about 100 m/s. The sea surface temperature (SST) and salinity were monitored in situ from the RV "Côte de la Manche" (CDLM) along the main part of the flight track (complete sampling in 7 days) with values ranging from 12.5°C to 15.5°C and 35.3 pss to 35.8 pss, respectively (Figure 1a). The wind conditions are summarized in Table 1 ranging from 4 to 15 m/s.

Table 1. Wind Conditions Measured by STORM and by the Meteorological Gascogne Buoy

Flight Time		STORM Data			Gascogne Buoy		
Day	Time (UTC)	Wspd (m/s)	Wdir (°/North)	nb	H_s (m)	Wspd (m/s)	Wdir (°/North)
19	05h45–10h50	5–13	150–270	43	4.2–3.5	5.6–7.5	190–240
22	18h40–23h10	4–9	300–30	68	1.5	2.7–7.2	330–0
25	18h30–22h50	9–15	310–30	63	3.0–3.6	9.8–11.5	340–0
27	05h20–07h20	10–14	310–10	10	2.5	9.4–10.8	330–350

The airplane took off from Brest (48.4°N–4.5°W) and flew over the Bay of Biscay (Figure 1) mainly by night (sunrise and sunset at, respectively, 7h40 and 16h30 UTC). Two flights occurred in the early morning (November 19th, 6h00–10h10 UTC and 27th, 05h30–07h15 UTC) and two in the evening (November 22nd, 19h00–23h00 UTC and 25th, 18h45–23h00 UTC). All the flights began westward up to the meteorological buoy Pharos at (48.5°N–5.6°W) (out-of-order during the campaign). The evening flights pursued southwestward up to (45.2°N–7°W) then eastward via the meteorological Gascogne buoy at (45.2°N–5°W) up to the Gironde mouth (45.5°N–1.6°W) and return to Brest via Gascogne and Pharos buoys. The morning flights followed the path Pharos, Gascogne, Gironde mouth for go and back except for on the 27th when the airplane continued after the Gironde mouth over the land up to Toulouse.

The aircraft attitude was measured by an inertial unit (a SAGEM sampling at 25 Hz) providing a relative precision better than 0.05° on the incidence angle (standard deviation on the roll angle of 0.04°).

2.2. CAROLS Radiometric Data

The CAROLS L-band radiometer [*Zribi et al*., 2011] was designed and built as a copy of the EMIRAD II radiometer [*Rotbøll et al*., 2003] constructed by the Danish Technical University team. It is a fully polarimetric and direct sampling correlation radiometer (sampling rate of 139.4 MHz). In this study, we use only the horizontal (H) and vertical (V) polarized antenna temperature (T_A), Th and Tv, respectively. The radiometric sensitivity is better than 0.1 K over 1 s integration time and the stability better than 0.1 K over 15 min before internal calibration [*Zribi et al*., 2011]. To assure measurement quality, an internal calibration is performed every 120–300 s according to the radiometer stability. This calibration has been improved since the previous study on CAROLS data over the ocean [*Martin et al*., 2012]. It now uses two internal loads with a Tb at 318 K (50 Ω load at 45°C) and at 54 K (using an Active Cold-FET Load) which is more adapted to radiometric measurements over the ocean (Tb between about 40 and 150 K). The antenna system includes a waveguide orthomode transducers and a Potter horn with a main lobe of 37° half-power beam width pointing at about 34° on the right-hand side of the aircraft.

A sequence of acquisition includes two steps: an internal calibration followed by an acquisition period. The internal calibration goes on for 20 s (10 s on each load). The acquisition period goes on for 120–300 s. This latter period is made up by 800 ms record of radiometric signal every second. The remaining 200 ms every second are not used. Raw data sampling is of 1 ms and includes kurtosis estimated from fast data acquired at a sampling rate of 139.4 MHz.

Postprocessing applied on raw data changed slightly compared to *Martin et al*. [2012] because using this latter postprocessing, we observe some remaining Radio-Frequency Interferences (RFI). The method to sort out observations possibly affected by RFI was based on a kurtosis criterion threshold. Only kurtosis between 2.9 and 3.1 is kept [Method F_K1 in *Pardé et al*., 2011]. Kurtosis criterion has been largely used for radiometric measurements e.g. [*Ruf et al*., 2006; *Skou et al*., 2010] but partly fails on our data since high T_A remains despite normal values of kurtosis (excess T_A up to 60 K in V-pol and 30 K in H-pol). In Appendix A, we proposed a modified algorithm for ocean radiometric measurements, which is more restrictive than the previous one. About 10% of the data integrated over 800 ms are flagged as RFI.

Full postprocessing applied on raw data consists of:

1. Correction for cable attenuation and reflection [*Zribi et al*., 2011].
2. Removing data flagged as RFI according to the algorithm described in Appendix A.
3. Computing the median T_A of each 800 ms block.

4. Removing data acquired at incidence angles more than $\pm 1^\circ$ away from the median incidence angle of each flight (boresight pointing at around 34°).

5. Averaging data on STORM time step (around 2 min).

According to the antenna aperture, altitude, and speed of the aircraft, the average radiometric footprint is about 2000 or 3000 $\times$ 12000 m^2.

2.3. STORM Radar Data

STORM is a C-band (5.35 GHz) scatterometer [*Mouche et al*., 2005; *Hauser et al*., 2008] from which estimates of sea surface wind speed and waves mean square slopes (mss) are derived. We recall below its main characteristics. STORM is a multipolarization radar, but in this study, we used only VV-polarized data. It includes a large antenna beam (30° in elevation plane and 7.6° in azimuth plane) pointing at 20° incidence angle and scanning in azimuth at about one turn per minute. The data processing provides a normalized radar cross section (σ^0) as a function of incidence angle every 1° from about 7° to 35° and as a function of azimuth directions every 0.4° over 360°.

Calibration of the radar was completed using ground target. Comparison of STORM estimated wind speed with Gascogne buoy wind speed lead to an additional bias correction of +1.54 dB.

We use the methods described in *Hauser et al*. [2008] to estimate wind speed and mss. Wind speed is estimated at 30° incidence angle using the empirical model CMOD2-I3 [*Bentamy et al*., 1994]. We choose this empirical model, because it has been calibrated with in situ observation, contrary to the latest empirical model CMOD5 [*Hersbach et al*., 2007], which has been fitted using ECMWF wind speed. Anyway differences of omnidirectional values of σ^0 between CMOD5, CMOD4, and CMOD2-I3 in the conditions of moderate wind speed and moderate incidence angles of our study are not significant [*Mouche*, 2005; *Hersbach et al*., 2007]. Differences in up/downwind and up/crosswind anisotropy between these models are more significant but do not affect the wind speed retrieval, since wind direction is derived without the use of any model and wind speed retrieval relies on the omnidirectional values.

At 30° incidence angle, signal measured by STORM is mainly caused by Bragg scattering from sea waves of about 5 cm. The mss is estimated through σ^0 variations between 7° and 16° incidence angle. This estimation assumes a modeling of σ^0 by geometric optics approximation and a Gaussian distribution of sea surface slopes. According to *Hauser et al*. [2008], estimated STORM mss are integrated over all wavelengths greater than 12 cm.

3. Excess T_A Induced by Sea Surface Roughness

To derive the excess antenna temperature induced by sea surface roughness (and foam), $T_{A,rough}$, we subtract T_A simulated for a flat sea (using flat sea emissivity model, adding atmospheric and galactic contributions, and including attitude correction), T_A^{mod}, from measured T_A ($T_{A,CAROLS}$), i.e.:

$$T_{A,rough}^{mes} = T_{A,CAROLS} - T_A^{mod}(\text{flatsea}), \tag{1}$$

where T_A^{mod} uses the same forward models as those used in *Martin et al*.[2012] and are integrated on CAROLS antenna pattern (whole front pattern) using the Terrestrial Radiometry Analysis Package developed by *Reul et al*. [2006, 2008]. Geophysical parameters needed to compute the forward model are obtained as follows: SSS and SST are derived from the CDLM in situ measurements (between 20 and 27 November) and extrapolated to the CAROLS ground track using a nearest neighbor method in space; atmospheric pressure and relative humidity are taken from the ERA Interim reanalysis [*Dee et al*., 2011] (6 h, 0.75° resolutions).

Measured $T_{A,rough}$ are compared with various simulated ones ($T_{A,rough}^{mod}$). These simulated $T_{A,rough}^{mod}$ are deduced from either empirical or physical models.

3.1. Physical Basis

Two main physical roughness models are used in L-band radiometry: a small perturbation method, small slope approximation (SPM/SSA), called here SSA [*Johnson and Zhang*, 1999], and a two-scale model. The two-scale model takes into account the tilting effect of large ocean waves on small waves (SSA

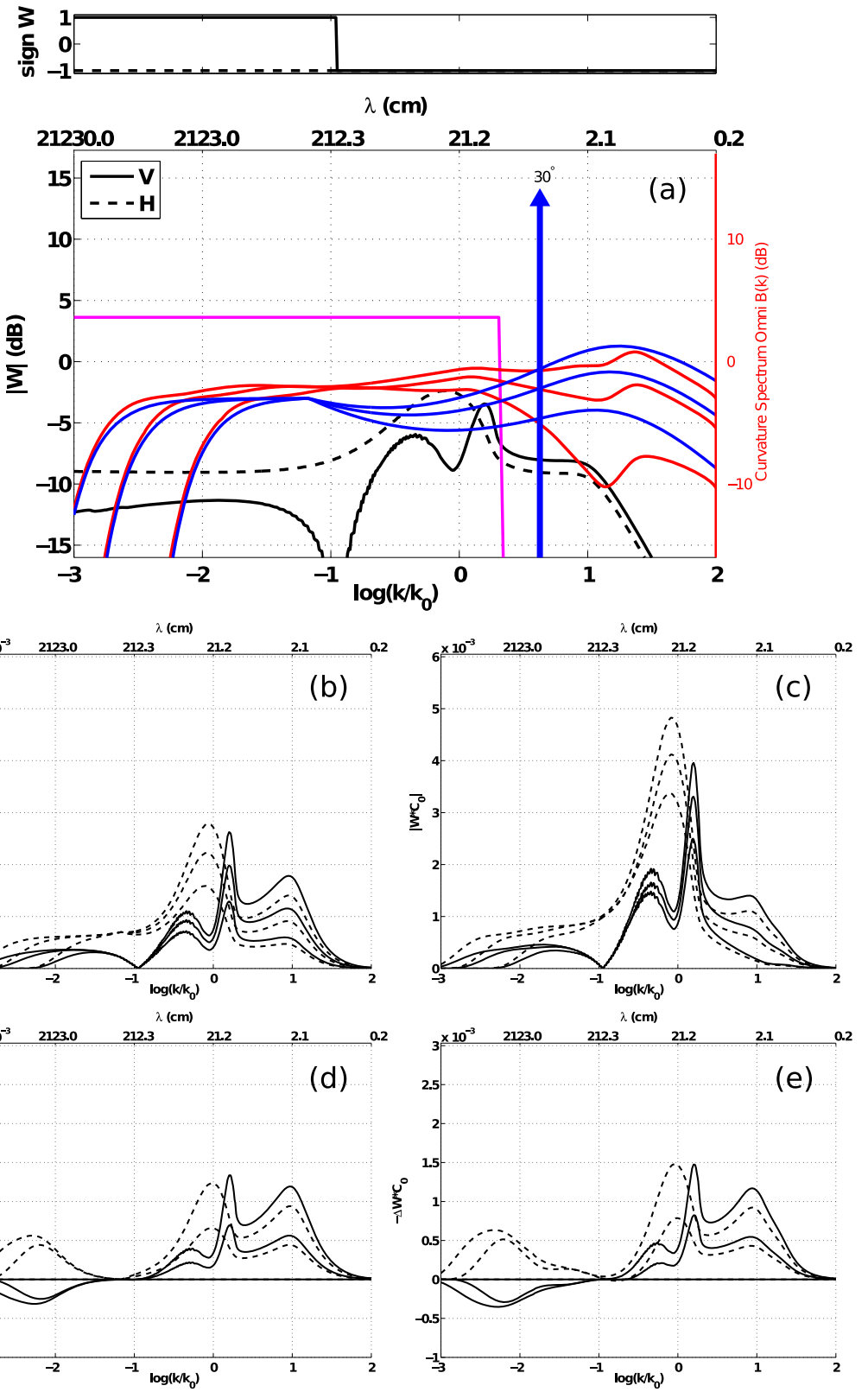

Figure 2.

parameterization) and add a hydrodynamic modulation of the waves [*Yueh*, 1997; *Dinnat et al.*, 2003]. Difference between Tb simulated with a given wave spectrum using either a two-scale or a SSA model is on the order of 0.1 K for omnidirectional component [*Dinnat et al.*, 2003].

Johnson and Zhang [1999] shows that $T_{A,rough}$ according to the SSA model is a function of the surface curvature spectrum filtered by a scattering weighting function over the roughness wavelength domain. An azimuthal harmonic decomposition permits to separate an omnidirectional and a second harmonic term. The weighting functions for both the omnidirectional and second harmonic terms are function of the incidence angle [*Johnson and Zhang*, 1999, Figures 1–3].

To analyze our data, the weighting functions have been integrated on CAROLS antenna pattern (Figure 2a) in both polarization for the omnidirectional component according to the following equation:

$$W_{\gamma,0}(\Theta)=\int_{\Theta-\pi/2}^{\Theta+\pi/2} G(\theta-\Theta).g'_{\gamma,0}(\beta,\theta).d\theta, \tag{2}$$

using same notations as in *Johnson and Zhang* [1999], with θ the incidence angle; $\beta=k/k_0$ the wavenumber k normalized by the electromagnetic wave number k_0; γ the H or V polarization; $g'_{\gamma,0}$ the nonintegrated weighting function; G the antenna gain pattern; $\Theta=34^\circ$ the CAROLS pointing incidence angle and $[\Theta-\pi/2;\Theta+\pi/2]$ the front pattern of the antenna.

The sign of the H-pol weighting function (Figure 2a, dashed line in the top) remains negative whatever the wave number. It implies that T_A increases when curvature spectrum increases, i.e., when wind speed increases. The amplitude of the H-pol weighting function (dashed line in Figure 2a) shows maximum between about 12 and 100 cm and plateau for waves between 2 and 12 cm and larger than 2 m. V-pol weighting function (solid line in Figure 2a) shows a lower and narrower maximum than in H-pol at about 12 cm, a higher plateau for small roughness scale (2–12 cm) and a moderate local maximum around 50 cm. However, large waves have a negative influence on T_A (positive weighting function) which tend to limit T_A increase with wind speed. Large waves have a lower absolute influence on V-pol than on H-pol. These weighting functions integrated on CAROLS antenna pattern (Figure 2a) are smoother than the 30° nonintegrated weighting functions [*Johnson and Zhang*, 1999, Figures 2c and 2d].

Using the same decomposition as in *Johnson and Zhang* [1999], we can derive an omnidirectional mss weighting function. We remark that this weighting function integrates homogeneously (in logarithmic scale) wave spectrum from largest wave scale up to 12 cm (Figure 2a in magenta).

To discuss wave spectrum impact on simulated $T_{A,rough}$, curvature spectrum multiplied by the CAROLS scattering weighting functions is represented in Figures 2b and 2c. We use two different wave spectra as example: *Durden and Vesecky* [1985] with its amplitude multiplied by a factor 1.25 (DV1.25) (blue curve in Figure 2a) as adjusted from SMOS data [*Yin et al.*, 2012; *Kudryavtsev et al.*, 2003] (KHCC) (red curve in Figure 2a). Both curvature spectra are similar for long wavelengths (>4 m) but differ significantly in the range 2–60 cm where the incertitude on the curvature spectrum remains large.

The roughness contribution $T_{A,rough}$ is derived from the integration of these curvature spectra on $log(k/k_0)$ [*Johnson and Zhang*, 1999]. Figures 2b and 2c point out that $T_{A,rough}$ is sensitive to roughness wavelengths from 100 m to about 1 cm. Although the maximum value of the weighted curvature spectrum is higher for KHCC (Figure 2c) than for DV1.25 (Figure 2b), the wind speed sensitivity in the range 5–13 m/s is quite similar (Figures 2d and 2e) for both conditions. These figures are analyzed more deeply in section 5.2.1.

Figure 2. (a) Weighting functions integrated on CAROLS antenna pattern at 34° for V (black plain line) and H (black dashed line) polarization. Curvature spectrum (DV1.25 in blue, KHCC in red) is plotted for wind speeds of 5, 9, and 13 m/s. The curves are in logarithmic scale (abscissa and ordinate) as function of wave number ratio (i.e., wave number normalized by the radiometer wave number). Weighting functions signs are plotted at the top of the figure. Purple rectangle indicates the range of wavelength onto which mss is integrated and the blue vertical arrow represents radar weighting function for VV polarization at 30° shifted by −88 dB. (b and c) Weighting function multiplied by the curvature spectrum for, respectively, DV1.25 and KHCC. All curves are as a function of wave number ratio. Signs are the same as for Figure 2a. (d) Difference between the curves at 9 and 13 m/s with the curve at 5 m/s represented in Figure 2b. (e) Same as Figure 2d for curves represented in Figure 2c. These last two figures represent the sensitivity of the filtered spectrum to the wind speed over the wavelength.

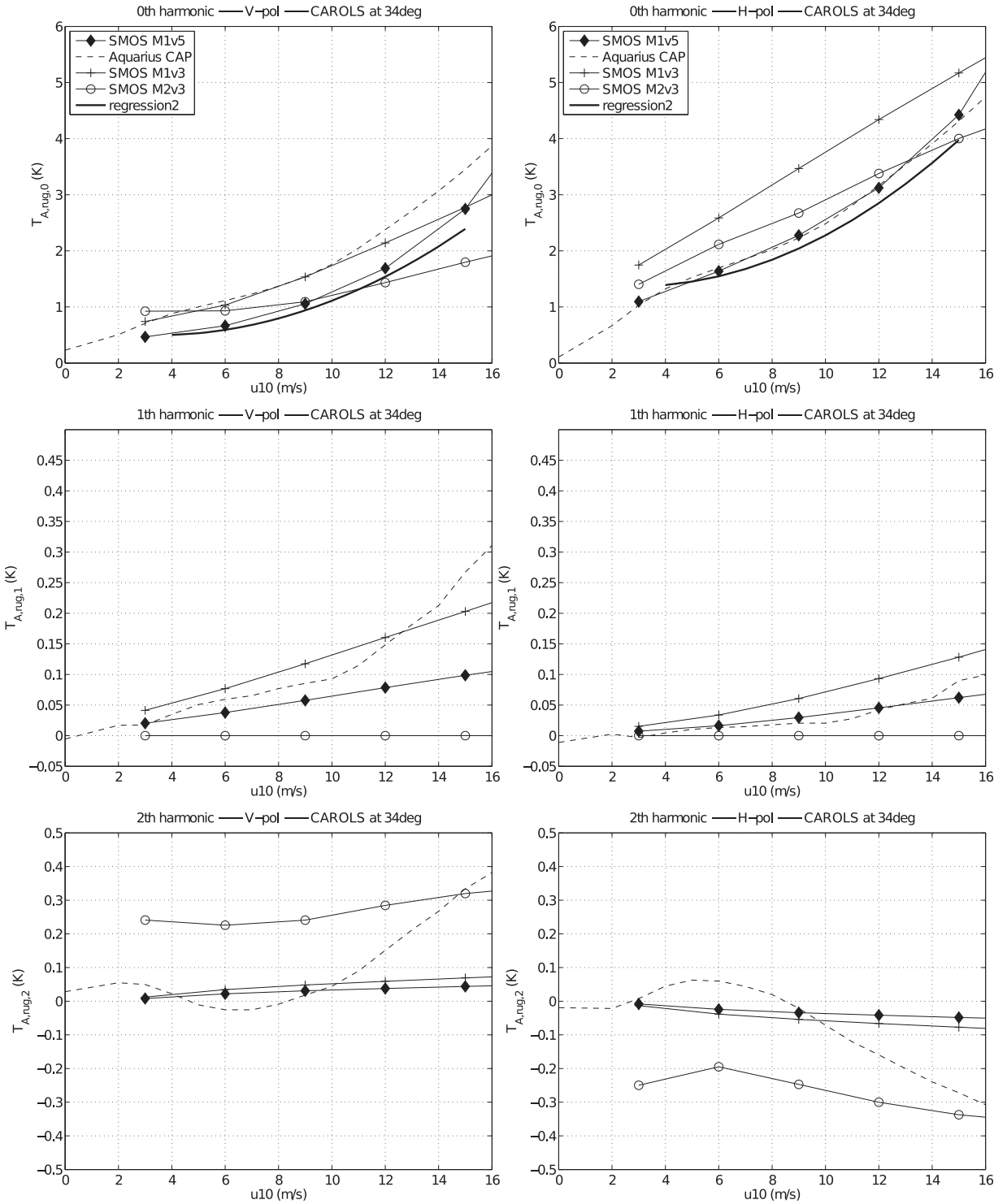

Figure 3. (top) Omnidirectional, (middle) first, and (bottom) second harmonics of wind azimuth of T_A induced by sea surface roughness for various forward models as a function of wind speed. (left) V-pol and (right) H-pol. Models are: SMOS M1v5 (black diamond), Aquarius CAP (dashed line), SMOS M1v3 (plus), SMOS M2v3 (circle), and regression2 (thick line).

3.2. Radiometric Roughness Models

Various models are used to simulate the excess T_A induced by the sea surface roughness and foam, called in the following (radiometric) roughness models. Four roughness models are compared here: three models used in various versions of SMOS data processing and one model used in Aquarius data processing. Two of

Table 2. Roughness Models Main Characteristics

Name	EM Model	Wave Spectrum	Foam	References
Aquarius CAP		Empirical		*Yueh et al.* [2013]
SMOS M1v5	Two scale	DV x1.2	Yes	*Yin et al.* [2012]
SMOS M1v3	Two scale	DV x2	No	*Dinnat et al.* [2003]
SMOS M2v3	SSA/SPM	KHCC	No	*SMOS Team* [2008]
regression2		Empirical		Figure 4

these are new models derived from satellite measurements, called here "Aquarius CAP" [*Yueh et al.*, 2013] and "SMOS M1v5" [*Yin et al.*, 2012] (used in ESA processor version 5) and two are SMOS prelaunch models, called "SMOS M1v3" [*Dinnat et al.*, 2003] and "SMOS M2v3" [*Johnson and Zhang*, 1999; *Kudryavtsev et al.*, 2003] (used in ESA processor up to version 3). The main characteristics of these four models are summarized in Table 2. The two new models which are derived from satellite measurements used two different wind products to derive these models. SMOS M1v5 used wind provided by ECMWF and Aquarius CAP used wind retrieved from SSMIS measurements. The wind reference does not show significant differences for SMOS M1v5 [*Yin et al.*, 2012, Figure 4].

Since differences between the three new SMOS roughness models are much less than differences between the SMOS prelaunch models M1v3, M2v3 and M1v5, only one of the three new models implemented in the ESA processor v5 is used in this study (M1v5). M1v5 includes an azimuthal dependence of Tb, contrary to the other two new (v5) SMOS roughness models. M1v5 is based on the same physical modeling foundations as M1v3 but with respect to M1v3, the amplitude of the wave spectrum and the dependence of the foam coverage with the wind speed have been adjusted in order to better fit SMOS measurements. The multiplicative factor applied to the wave spectrum was reduced from 2 in M1v3 to 1.25 in M1v5.

$T^{mod}_{A,rough}$ are integrated on CAROLS antenna pattern for the three SMOS models. For the Aquarius CAP model that is only available for the three Aquarius incidence angles (about 29°, 38°, 46°), we interpolate linearly the Aquarius CAP coefficients to CAROLS boresight incidence angle.

The four satellite roughness models can be decomposed as cosine series of wind azimuth relatively to antenna boresight (φ):

$$T^{mod}_{A,rough,p}(U,\varphi) = T^{mod}_{A,rough,p,0}(U) + T^{mod}_{A,rough,p,1}(U).\cos\varphi + T^{mod}_{A,rough,p,2}(U).\cos 2\varphi, \quad (3)$$

with p the polarization (H or V) and U the wind speed. Omnidirectional ($T^{mod}_{A,rough,p,0}$), first ($T^{mod}_{A,rough,p,1}$), and second ($T^{mod}_{A,rough,p,2}$) harmonics components integrated on CAROLS antenna pattern (except for the Aquarius CAP) are plotted in Figure 3. An empirical relationship found from the CAROLS data is also shown in Figure 3. It was obtained from a fit by a second-order polynomial of $T_{A,rough}$ with STORM wind speed, and is called in the following "regression2" (see details in next section). It does not take into account any azimuthal dependence and it was obtained with wind speed derived from STORM measurements during the campaign going from about 3 to 15 m/s.

Variations of $T^{mod}_{A,rough,p,0}$ with wind speed obtained with the SMOS M1v5 and the Aquarius CAP new roughness models in the 3–15 m/s range are in rather good agreement, both models showing a quadratic dependence with wind speed for both polarizations (Figure 3, top). In contrast, SMOS M1v3 and M2v3 models exhibit a quasi-linear dependence with wind speed. This is because in opposite to M1v5 and CAP models, they neglect influence of foam. There are large differences in wind speed sensitivity in comparison with the M1v5 and CAP, particularly for M2v3 in V-pol and M1v3 in H-pol at moderate wind speed ($<$10 m/s). The empirical model, called regression2 (see next section for details) is much closer to M1v5 and CAP models than to the prelaunch SMOS models. However, it presents a slightly lower sensitivity to wind speed than M1v5 and CAP on the range wherein the fit was computed.

For all models, the contribution of the first and second harmonics is much less than the omnidirectional component (less than 10% of $T^{mod}_{A,rough,p,0}$ for the new models), being only a fraction of a Kelvin at most wind speeds. The first harmonic's influence is larger in V-pol than in H-pol for all models, (note: M2v3 and regression2 do not include this harmonic). There is a good agreement between SMOS M1v5 and Aquarius CAP $T^{mod}_{A,rough,1}$ in H-pol and in V-pol up to 11 m/s.

The second harmonic has a very small (less than 0.1 K) influence for SMOS M1v3 and M1v5, and for Aquarius CAP up to 11 m/s. Of note, $T^{mod}_{A,rough,2}$ for Aquarius CAP and SMOS M1v5 are of opposite sign in the range

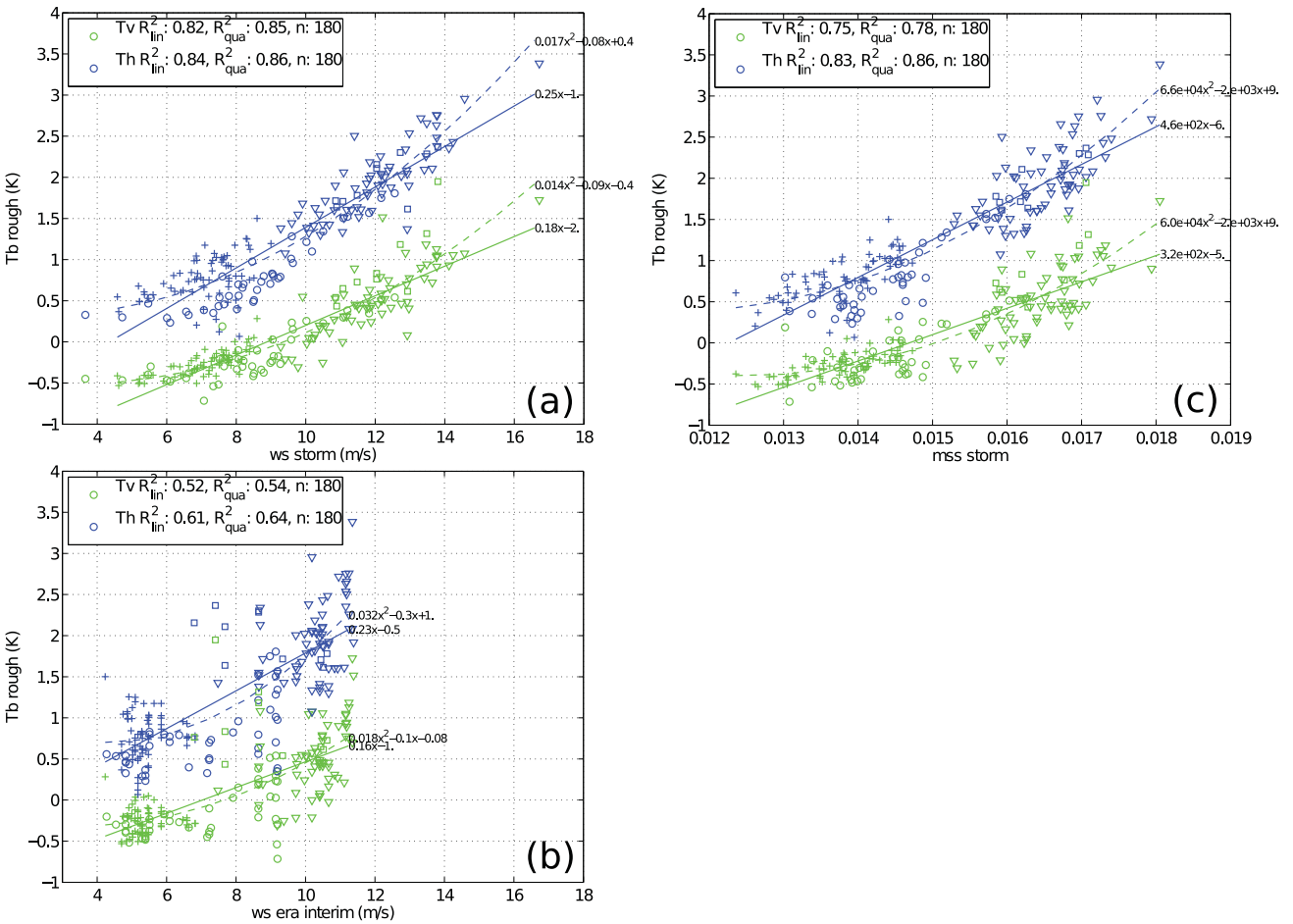

Figure 4. $T_{A,rough}$ as a function of (a) STORM wind speed, (b) Era Interim wind speed, (c) STORM MSS. R^2 coefficient using a linear (R^2_{lin}) or quadratic (R^2_{qua}) dependency with wind speed or mss and the number of data are indicated in the inset of each figure. Linear and quadratic regression coefficient is indicated on the plots. The four flights are represented with four different symbols, in chronological order of flights: circle, plus, triangle, and square.

4–9 m/s, because the CAP model changes sign. SMOS M2v3 shows a much larger influence of the second harmonic in comparison with other models up to 15 m/s, and comes in a relative closer agreement with the Aquarius CAP model at the largest wind speeds.

Effects of roughness model integration on CAROLS antenna pattern was tested with the three SMOS models presented here. The main difference with the nonintegrated model for the omnidirectional component is a positive and quasi constant bias in H-pol (0.2 K using SMOS M1v5) and a negative bias and trend with wind speed in V-pol (0.2 K at 5m/s and −0.03 K/(m/s) using SMOS M1v5) and slightly positive in H-pol (not shown). This could partly explain the positive bias in $T^{mod}_{A,rough,V,0}$ for Aquarius CAP compared to SMOS M1v5 (Figure 3) while uncertainties on the absolute calibration of the radiometers could also create such differences. The effect of the integration for the first harmonic indicates that Aquarius CAP $T^{mod}_{A,rough,1}$ should be increased with respect to the value shown in (Figure 3); hence Aquarius CAP first harmonic is higher than other models, especially at high wind speed. There is no significant effect of integration on the CAROLS antenna pattern for the second harmonic for any of the three models.

To avoid problems due to absolute calibration of radiometric measurements, models offset or the nonintegration of CAP on the CAROLS antenna pattern, we centered each measured or simulated $T_{A,rough}$ by the mean on the whole campaign where CAROLS and STORM data are available.

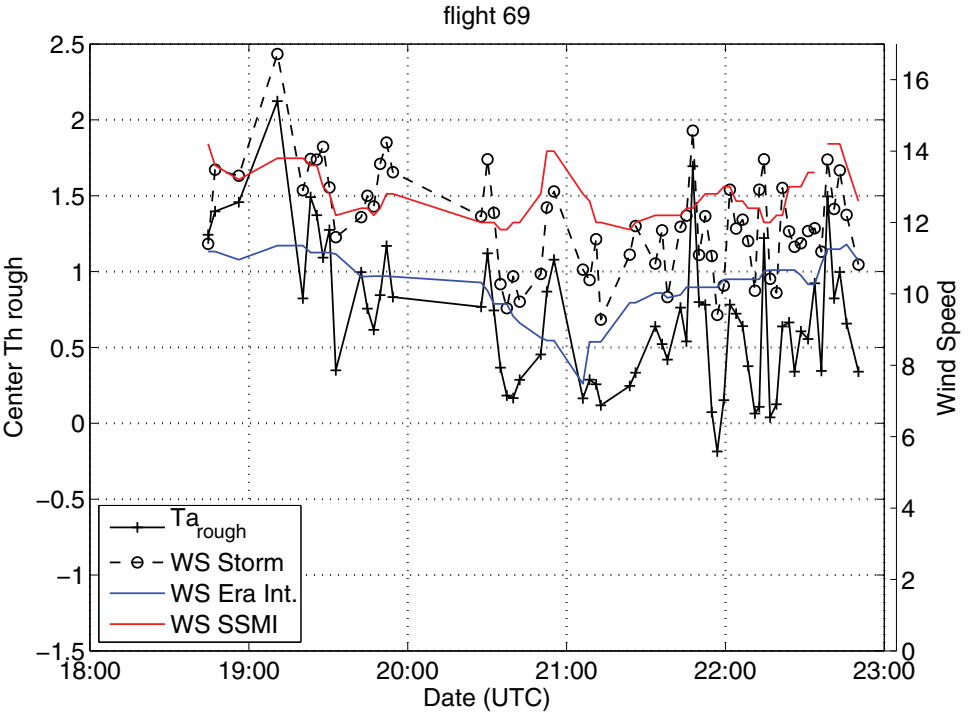

Figure 5. $T_{A,rough}$ (solid line and plus symbol, in K) and wind speed (in m/s) temporal evolution along the flight track for the flight 69 (25 November 2010). STORM wind speed in dashed line and circle symbol, ERA Interim wind speed in blue and SSMI wind speed in red. SSMI wind speed is collocated with the nearest neighbor value in time (90% at less than ±3.6 h).

4. Results Using Synergy Between CAROLS and STORM Observations

4.1. Excess T_A Versus STORM and ERA Interim Roughness Parameters

Excess antenna temperature due to roughness has been estimated using the CAROLS data set (180 data points over four flights) using equation (1) and related to wind or mss derived from the STORM measurements (colocated and at the same scale) or wind provided by the ECMWF ERA Interim wind fields reanalysis (Figure 4). Linear and quadratic regression has been computed to determine which parameter is best suited to explain $T^{mes}_{A,rough}$ variations at the first order. A quadratic function of STORM wind speeds explains more than 85% of the $T^{mes}_{A,rough}$ variance for both polarizations, whereas the one derived with ERA Interim wind speeds explains less than 64%. Figure 4b highlights a weak dynamic range of ERA Interim wind speeds, mostly concentrated around 5 and 10 m/s; this could be the reason for the poorer performance at explaining our measurements compared to STORM wind speeds. STORM mss achieves similar performance as STORM wind speed to explain H-pol variability but is slightly worse in V-pol (still much better than ERA Interim).

Figure 5 shows STORM wind speed and $T^{mes}_{A,rough}$ along the flight track for the 25 November 2010 flight. It highlights the high spatiotemporal variability of wind speed and resulting $T^{mes}_{A,rough}$ sampled up to every 2 min and 12 km. Wind speed can change by more than 4 m/s over just a few minutes/dozen km. Wind speed reanalysis and satellite measurements (SSMIS data considered) are not able to sample the variability measured by the airborne scatterometer STORM (Figure 5). Having simultaneous measurements of sea surface roughness (e.g., wind speed) for interpreting L-band radiometric measurements are a great help. In the following of the paper, STORM wind speed and wind direction will be used to compute $T^{mod}_{A,rough}$.

4.2. Measured and Simulated T_A

Comparisons of centered $T^{mes}_{A,rough}$ and $T^{mod}_{A,rough}$ give correlation (Pearson coefficient) higher than 0.9 in H and V-pol for all models except SMOS M2v3 (Table 3). The root-mean-square (rms) difference is the lowest for regression2 even though this empirical model does not take into account any azimuthal component. SMOS M1v5 rms difference is smaller than that of SMOS M1v3, especially in H-pol. Aquarius CAP has a slightly larger rms difference than SMOS M1v5, perhaps due to a nonintegration on CAROLS antenna pattern. SMOS M2v3 is not as good as other models, particularly in V-pol. Part of the rms difference could be associated to scaling

Table 3. Centered $T_{A,rough}$: CAROLS Versus Models ($n = 180$)

	Correlation		rms Difference (K)	
	H	V	H	V
Aquarius CAP	0.92	0.91	0.29	0.25
SMOS M1v5	0.92	0.91	0.27	0.21
SMOS M1v3	0.91	0.90	0.31	0.22
SMOS M2v3	0.88	0.70	0.32	0.37
regression2	0.93	0.92	0.25	0.20

effect of the nonlinear relation between T_A and wind speed. Indeed, SMOS and Aquarius models have been fitted with a footprint of about 50–150 km, whereas the aircraft integrated footprint is about 2 × 12 km. For each model, the rms difference is about one order of magnitude higher than expected from the radiometric noise only (NEDT < 0.02 K over 2 min integration time).

4.3. Residuals Analysis

In the previous section, we pointed out good agreement between measured and simulated $T_{A,rough}$ but with a rms difference higher than expected from instrument noise alone. To interpret these differences, we analyze the part of $T^{mes}_{A,rough}$ signal that is not explained by the roughness-component of the models $T^{mod}_{A,rough}$, i.e., the residuals defined as the difference between measurement and model after removing the mean value on the whole campaign:

$$\Delta T_{A,rough} = \left(T^{mes}_{A,rough} - \overline{T^{mes}_{A,rough}}\right) - \left(T^{mod}_{A,rough} - \overline{T^{mod}_{A,rough}}\right), \quad (4)$$

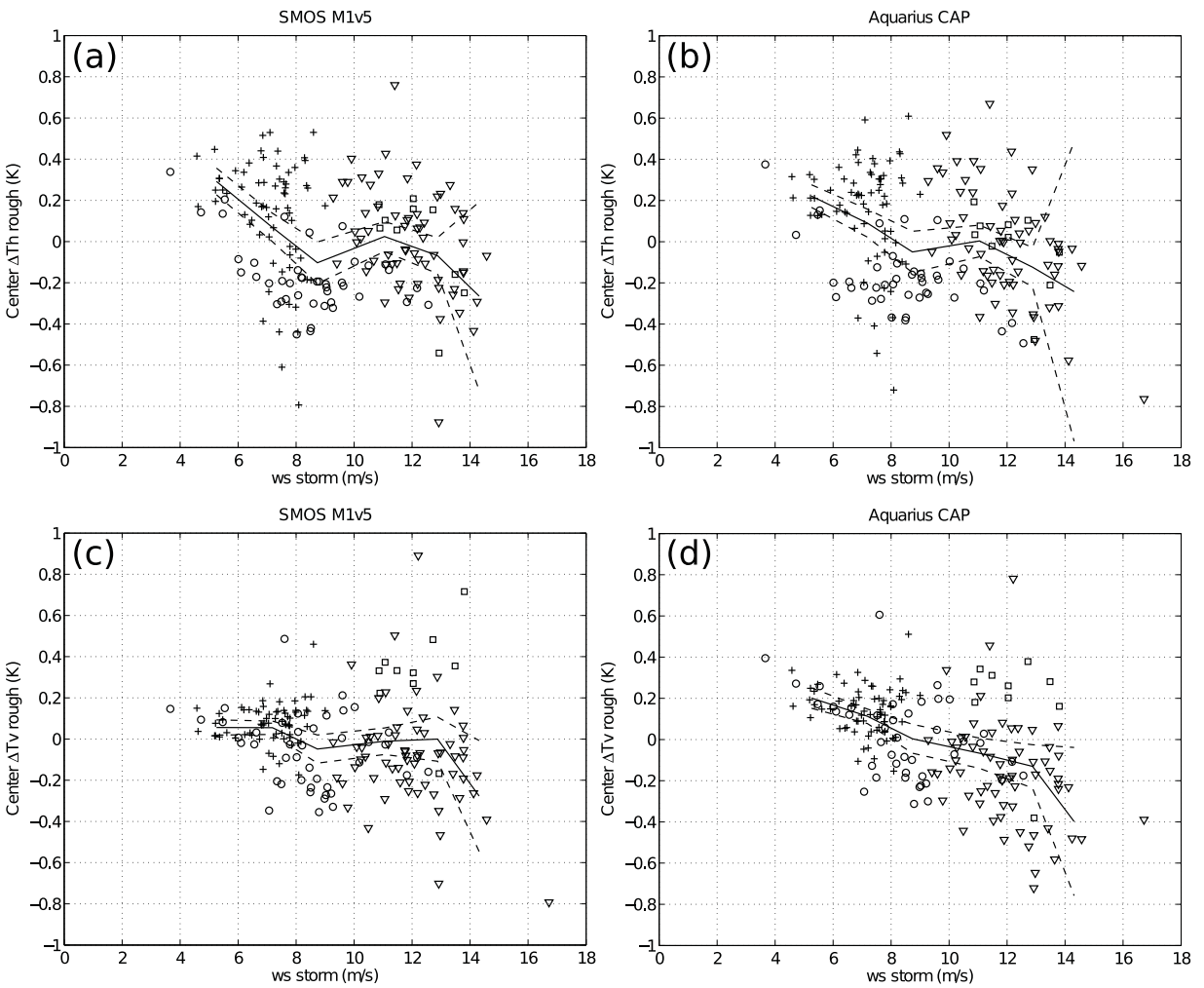

Figure 6. $T_{A,rough}$ residuals in H-pol as a function of STORM wind speed using (a) SMOS M1v5 and (b) Aquarius CAP models. (c and d) Same as Figures 6a and 6b but for V-pol. The solid line indicates the estimate of the mean and dashed lines the confidence intervals, assuming a normal distribution. Means and confidence intervals are calculated at 2 m/s intervals. The four flights are represented with four different symbols, in chronological order of flights: circle, plus, triangle, and square.

Table 4. Regression Slope Between Residuals and First or Second Harmonics, When It Is Significant at a Level Better Than 99.9%[a]

	Regressed Variable	WS Range (m/s)	Pol.	Regression Slope	Contribution at 9 m/s
Aquarius CAP	$\cos\varphi$	<9	V	−0.053 to −0.146	0.085
SMOS M1v3	$\cos\varphi$	<9	V	−0.054 to −0.154	0.117
SMOS M2v3	$\cos 2\varphi$	All	H	0.305 to 0.198	−0.247
SMOS M2v3	$\cos 2\varphi$	All	V	−0.226 to −0.350	0.241

[a]Last column recalls the value of the first and second harmonics for a wind speed of 9 m/s.

where $\bar{X}$ indicates data averaging over the whole campaign. In the following, we analyze the $T_{A,rough}$ residuals as function of wind speed and wind direction. If roughness models are correct, the residuals should not depend on these two parameters.

4.3.1. Residuals Dependency on STORM Wind Speed

$\Delta T_{A,rough}$ obtained with SMOS M1v3 and M2v3 follow a quadratic dependency with wind speed (not shown) since the quasi-linear dependence with wind speed of these models do not reproduce the quadratic dependence highlighted in Figure 4a. In addition, the residuals reveal that SMOS M2v3 tends to underestimate wind speed sensitivity in V-pol by about 0.1 K/(m/s) and SMOS M1v3 tends to overestimate wind speed sensitivity in H-pol up to about 9 m/s by about 0.1 K/(m/s) (not shown). Aquarius CAP and SMOS M1v5 residuals are much lower and do not show such a clear dependency on wind speed (Figure 6). Hence, these CAROLS results confirm the main improvements of the new SMOS and Aquarius models with respect to the prelaunch SMOS models. However, Aquarius CAP residuals in V-pol present a slight negative slope with wind speed which indicates a slight overestimation of wind speed dependency (Figure 6d) of about 0.02 K/(m/s). We remark a lower scattering of the data in V-pol for moderate wind speed (<9 m/s) (std of about 0.15 K) than for higher wind speed (std >0.25 K). We find this feature again with SMOS M1v5 and regression2 residuals in V-pol (Figure 6c). In H-pol, regression2, SMOS M1v5, and Aquarius CAP residuals have a std slightly higher than in V-pol, although less than 0.3 K whatever the wind speed. Despite this high noise, residuals of Aquarius CAP and SMOS M1v5 tend to show a slight underestimation of the wind speed correction for low wind speed (<7 m/s) (Figures 6a and 6b).

4.3.2. Residuals Dependency on Wind Azimuth

Regression2 residuals do not significantly depend on the first and second harmonic of the wind direction whatever the range of wind speed (not shown) although regression2 has no dependency with wind direction. To assess the absence of significant wind azimuthal dependency on $T_{A,rough}$, we analyze residuals of the four other models which take into account a wind direction dependency. $\Delta T_{A,rough}$ obtained with models reported in Table 4 are significantly correlated (better than 99.9%) with $\cos\varphi$ or $\cos 2\varphi$ for various wind speed range (Table 4). 95% confidence intervals of linear regression slope are indicated in the table. The slopes obtained are about opposite to the $T^{mod}_{A,rough}$ correction for the first or second harmonic (Figure 3, and reported in Table 4 for a reference wind speed of 9 m/s).

SMOS M1v3 and Aquarius CAP residuals present linear regression slope along $cos\varphi$ for moderate wind speed (<9 m/s) opposite and of about the same order of magnitude as the first harmonic. This suggests an undetectable first harmonic signature on our CAROLS data. For higher wind speed, our data set and large residual noise do not permit to conclude despite strong differences between models in V-pol (Figure 3c). In H-pol, no significant influence is observed relatively to the first harmonic for any roughness model.

The second harmonic is too large for M2v3 whatever the polarization and wind speed range (Table 4). Residuals correlation with $\cos 2\varphi$ is higher (>0.6 in absolute value) for moderate wind speed (<9 m/s) than for higher wind speed (correlation of 0.5). Aquarius CAP second harmonic in both polarization tend to be slightly too large at high wind speed (>9 m/s); although residuals correlation is weak (around 0.3) it is significant at a confidence level of 99%.

4.3.3. Residuals Dependency on mss Anomaly

For a fully developed wind-sea, there is a unique relation between wind speed and mss. In reality, sea is never fully developed and integrates wind variation's history (changes in speed and direction). These

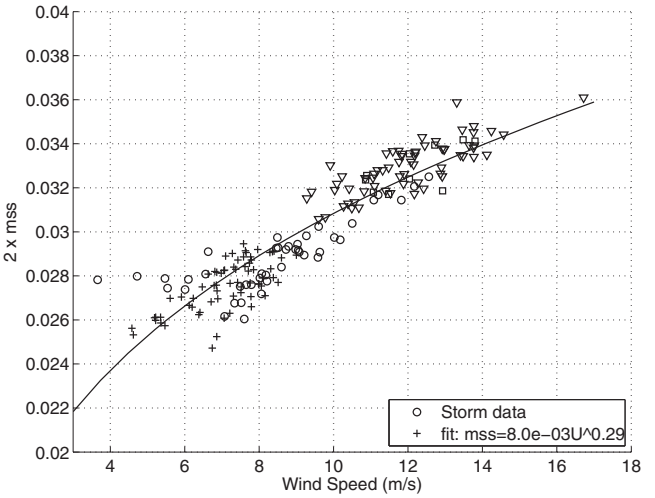

Figure 7. STORM total effective mean square slope as function of STORM wind speed. Black curve fits data according to a power law (coefficient indicated in the legend). The four flights are represented with four different symbols, in chronological order of flights: circle, plus, triangle, and square.

variable conditions affect differently the various wave roughness scales. Small scales tend to fluctuate more rapidly than larger scales. As STORM-derived wind speed and mss are sensitive to different roughness scale, we define the mss anomaly as the deviation of mss from a fit between mss and wind speed derived from all STORM measurements (Figure 7).

As L-band radiometry is sensitive to a large range of roughness scale [*Johnson and Zhang*, 1999], our aim is to study if we could evidence a relationship between mss anomaly and radiometric signal. In the following, we will define small scales as the wavelengths smaller than 10 cm, medium scales the wavelengths between 10 cm and 10 m, and large scales the wavelengths above 10 m.

This comparison between radiometric signal and mss anomaly is shown in Figure 8, left. It shows a positive correlation between $T_{A,rough}$ residuals in H-pol and mss anomaly. Two distinct point clouds appear, with a split at a mss negative anomaly value of about 4×10^{-4}. T_A difference between the two point clouds (distribution peak, Figure 8, right) is about of 0.3 K. We found similar feature for Aquarius CAP and SMOS M1v5 models. In V-pol, no significant relation is found between $T_{A,rough}$ residuals and mss anomaly for any model.

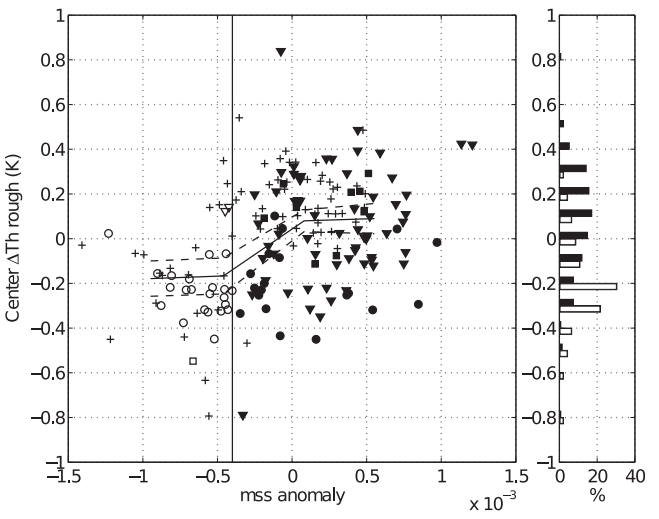

Figure 8. (left) $T_{A,rough}$ residuals as a function of mss anomaly in H-pol for regression2 model and for all wind speeds (symbols in white and in black). The solid line indicates the estimate of the mean and dashed lines the confidence levels, assuming a normal distribution. Means and confidence levels are calculated at 6×10^{-4} mss anomaly intervals, provided there are more than five points. The four flights are represented with four different symbols, in chronological order of flights: circle, plus, triangle, square. The vertical line indicate mss anomaly of -4×10^{-4}. (right) Histogram of $T_{A,rough,H}$ residuals for mss anomaly (%). Empty symbols and white bars correspond to mss anomaly lower than -4×10^{-4} and filled symbols and black bars to higher values.

5. Discussion

In the above analysis, we implicitly consider differences between measured and simulated T_A as originating from imperfections in the roughness models. However, T_A residuals potentially contain errors on all other components of the forward model, radiometric measurements errors being expected to be an order of magnitude smaller. We now investigate the order of magnitude of potential errors on each model component other than roughness before discussing results of T_A residuals analysis.

5.1. Error Sources

5.1.1. Flat Sea Model

The emissivity model for a flat sea depends on sea surface

dielectric constant (related to SSS and SST) and incidence angle. Differences in $T_A^{mod}(\text{flatsea})$ simulated with various dielectric constant models [*Meissner and Wentz*, 2012; *Lang et al*., 2010; *Blanch and Aguasca*, 2004] relative to the *Klein and Swift* [1977] model (used here) is always less than 0.06 K after removing mean campaign bias according to the campaign sea surface condition. We estimate also a maximum error in our extrapolated SSS and SST at ocean fronts of the order of 0.2 pss and 1°C. It results in T_A error of less than 0.1 K on few areas. Error due to relative uncertainty on incidence angles ($<0.05°$) could bring errors in T_A lower than 0.07 K in V-pol, and 0.04 K in H-pol. Errors on roll and pitch angles being roughly Gaussian, the averaging process should reduce again the noise from attitude.

5.1.2. Atmospheric Model

Root-mean-square error on atmospheric pressure (the atmospheric parameter that has the strongest impact on Tb at L-band) from Era Interim reanalysis is of the order of 1 hPa [*Dee et al*., 2011], introducing an error on T_A less than 0.01 K.

5.1.3. Galactic Signal

A study led by J. Tenerelli (personal communication, 2011) points out that effective galactic signal scattered by sea surface is in fact intermediate between specular reflection from a flat sea and the output of the scattered model [*Tenerelli et al*., 2008] for a wind speed of 3 m/s. In our study, scattering of the galactic signal was estimated with *Tenerelli et al*. [2008] model forced by the STORM wind speed, always higher than 3 m/s. Hence, the scattering by the sea surface is expected to be much overestimated. In order to bound the error on the simulated scattered galactic signal, we compute the difference between our scattered estimate and the specular reflection of the galactic signal. Differences are up to 0.36 K for T1 ($=T_v+T_h$) with a standard deviation of 0.1 K. Only one flight direction (airplane flying southwest, 15% of the data set) in the evening shows differences higher than 0.2 K. These data correspond to Cygnus and Cassiopeia reflected in CAROLS main lobe. Removal of these data does not change significantly results shown in previous sections neither standard deviation value of T_A residuals.

5.1.4. Neglected Parameters

In the forward model, we neglect influence of sun, rain, and swell. Flights have been planned to have no influence of the sun (night flight). Only two and half hours of measurement of the first morning flight (19 November) occurred after the sun rise. T_A residuals do not highlight significant signal when sun or rain (<4 mm/h according to SSMIS) occurred. In all the four flights, sea state was characterized by either wind-sea or mixed sea conditions (swell + wind-sea) as indicated by the WaveWatch3 model run by the PREVIMER forecast system [*Lecornu and De Roeck*, 2009]. However, adding swell to the wind-sea wave spectrum in the forward model (SMOS M1v3) does not change T_A by more than 0.03 K for incidence angle between 0° and 50°. This model has been developed and validated at higher frequency [*Yueh*, 1997] and needs to be validated for L-band. The model includes hydrodynamic modulation as a function of the mean square slope.

5.2. T_A Residuals Analysis

5.2.1. Wind Speed and Direction Influence

We find that simulations performed with roughness models that take into account quadratic dependence on wind speed better compare with CAROLS measurements. This quadratic dependence is either obtained using a foam parameterization (SMOS M1v5) or empirically (Aquarius CAP and regression2).

Independently to this aspect, we discuss here differences between analytic models (i.e., SMOS M1v3, M1v5, and M2v3) to understand the impact of the various roughness scales on the signal. This discussion is not suitable for empirical model in which all roughness scales are integrated. To that purpose, we deepen the analysis began in section 3.1 on the weighting functions and on the wave spectra (Figure 2). Wave spectra DV1.25 and KHCC are similar for high wavelengths (>4 m) but show differences in the range 2–60 cm (Figure 2a). KHCC shows higher value in the range 10 cm to few meters than DV1.25 but with a lower dynamic range with changes in wind speed. Therefore, the peak in the H-pol filtered KHCC (Figure 2c) is higher than for DV1.25 (Figure 2b), but the sensitivity to wind speed (area differences between curves) is similar in this wavelength range. In the wavelength range 1–10 cm, wave spectra vary differently from each other (Figure 2a), but the sensitivity to wind speed is similar, bringing almost similar sensitivity to the filtered wave spectra (Figures 2d and 2e). Without taking into account foam impact, KHCC and DV1.25 wave spectrum simulate same wind speed sensitivity in H-pol (in agreement with Figure 3b, with SMOS M2v3—KHCC wave spectrum—and M1v5 at wind speeds lower than 10 m/s to limit foam's influence). In V-pol, the higher dynamic of DV1.25 compared to KHCC makes the

Table 5. Changes in T_A and Filtered mss Variations According to Observations and Models for a Young Sea ($\Omega=2$) Compared to (Minus) a Fully Developed Sea ($\Omega=0.84$)

	Observation		ECKV		KHCC	
δmss_{eff}	−0.002		−0.005		−0.003	
$\Delta T_{A,rug}$ (K)	H	V	H	V	H	V
	≈ -0.3	≈ 0	≈ -0.6	$\approx +0.3$	[−0.5; 0]	[0; +0.5]

difference of sensitivity (out of foam) between SMOS M1v5 and SMOS M2v3. SMOS M1v3 uses the DV2 wave spectrum, i.e., a wave spectrum 60% higher than DV1.25. Wind speed sensitivity of SMOS M1v3 is therefore 60% higher than SMOS M1v5 at moderate wind speed (i.e., when foam can be neglected). This analysis points out the importance of having a good parametrization of wavelengths between 1 cm and about 1 m.

Regarding the wind direction influence, our data set does not show an azimuthal signal related to the wind direction. *Yueh et al*. [2010] show a wind azimuthal influence which is significant for wind speed of 14 m/s and higher. In our data set, only four measurements occurred with a wind speed higher than 14 m/s which is insufficient to conclude. Nevertheless, we point out a too large sensitivity of the second harmonic of SMOS M2v3 which is likely due to a too high value of the second harmonic of KHCC curvature spectrum at wavelength higher than 10 cm [*Guimbard*, 2010, Figure E.3] where the second harmonic weighting function shows a plateau [*Johnson and Zhang*, 1999, Figure 2a]. We find that the wind direction influence on T_A has to be smaller than 0.2 K, our residual noise, for wind speeds less than about 12 m/s (75% of data set).

5.2.2. Medium and Large Roughness Scale Influence

One important result of this study is to point out a T_A double dependency in H-pol on wind speed (centimeter roughness scales) and to filtered mss (which takes into account all scales higher than 12 cm). We interpret this double dependency as a quicker response of small roughness scales to local wind speed than that of medium and large roughness scale. This may happen in case the sea is not fully developed, either for a developing sea or a decreasing sea, or in response to variations in local wind compared to the averaged wind. We test the impact of a developing sea on T_A and mss using two wave spectrum models, KHCC and [*Elfouhaily et al*., 1997] (ECKV), which simulate wave spectrum according to sea development, i.e., time (or space) since wind blows, through the wave age parameter. The results are presented in Table 5.

According to the ECKV wave spectrum, wave age (young sea versus mature sea) impacts mainly wavelengths higher than 60 cm. Thus, it affects more largely H-pol (positively) than V-pol (negatively), for which weighting functions exhibit a plateau at high wavelengths (Figure 2a). T_A simulated for a young sea (inverse wave age $\Omega=2$) compared to T_A simulated for a fully developed sea is decreased by about 0.6 K in H-pol and increased by about 0.3 K in V-pol.

Wave age influence on KHCC wave spectrum is based on the ECKV model for the larger scales, but it increases (nonuniformly) the wave spectrum for a young sea in the range from 5 to 6 m. It results in a V-pol T_A increasing by 0.5 K for a young sea. In H-pol, there is a small decrease for a young sea at low wind speed; the reduction in T_A becomes larger above around 7 m/s (up to about 0.5 K).

Filtered mss decrease for a young sea by about 0.005 (ECKV wave spectrum) and 0.003 (KHCC wave spectrum) whatever the wind speed is.

In summary, simulations with ECKV wave spectrum are in qualitative agreement with Figure 8, with a positive correlation of T_A and mss variations and with a higher response in H-pol than in V-pol.

However, the ECKV wave spectrum variations which explain T_A variation are related to relatively large scales of roughness which take time to develop (a few hours). We observe these variations at large spatiotemporal scales (1 h, 100 km) but also at smaller scales (5 min, 20 km). This suggests that wave age is not sufficient to explain mss and T_A variations, but that one should probably also take into account local variation of wind (e.g., wind gust) or other parameters such as sea surface currents.

These results have been obtained at an incidence angle of 34° for an antenna pattern of 37° half-power beam but we can extrapolate them to general incidence angle thanks to the *Johnson and Zhang* [1999] weighting functions. At nadir, we expect to have no sensitivity to large wave scales (mss) [*Johnson and Zhang*, 1999,

Figure 1c] whereas at large incidence angle (60°), we expect to be highly sensitive to large wave scale with an opposite variation between the H and V polarization [*Johnson and Zhang*, 1999, Figure 3c].

6. Conclusion

Using collocated L-band radiometric and scatterometer observations, we found that the roughness contribution to the L-band antenna temperature may be parameterized at the first order (explaining 85% of the variance) by a quadratic law in wind speed. The model is in agreement with the most recent models used for the roughness correction on SMOS data, which include foam effects, as well as one of the models derived from Aquarius measurements. We also show that collocating meteorological model wind fields (at 6 h, 0.75° resolution) to airborne radiometer data is not well suited to study the roughness contribution to T_A (Era Interim explains only 65% of the variance). The quadratic empirical model (regression2) based on the campaign data set, although not taking into account any wind direction influence, gives slightly better statistical results than the most recent satellite roughness models (Aquarius CAP and SMOS M1v5). This is probably explained by the fact that the satellite models are derived using a global data set under varying roughness conditions while regression2 uses a more limited regional data set and the fact that the statistical results mentioned above have been obtained using data used to perform the fit. As a consequence, it is possible that the improved performances of the latter model for the particular region under study translate into less versatile performances at global scales.

To understand the performance of the various roughness models, we analyze the residuals between CAROLS and various forward models. At low to moderate wind speeds, medium to large roughness scales (estimated through STORM mss) have a similar (even higher sometimes) impact on the antenna temperature than wind direction. We confirm this link between medium and large roughness scales and T_A theoretically, according to wave age, using the [*Elfouhaily et al*., 1997] and [*Kudryavtsev et al*., 2003] wave spectra. These models using only a wave age parameterization are probably too simple to describe the observed ocean sea state. Further study using numerical wave models such as WaveWatch III [*Tolman*, 2009] and local parameters to simulate realistic wave spectrum, and therefore realistic T_A and mss, would be interesting. Residuals analysis also indicates for Aquarius CAP a too high first harmonic of wind direction in V-pol for wind speed lower than 9 m/s and a slightly too large second harmonic for wind speed higher than 9 m/s in both polarizations. It shows also a slight overestimation of the omnidirectional wind speed correction on T_A in V-pol of about 0.02 K/(m/s) but this could be due to the nonintegration on CAROLS antenna pattern. No significant dependency of residuals on wind speed or wind direction is observed when using SMOS M1v5. These conclusions are based on the relatively limited data set acquired in the Gulf of Biscay during the CAROLS experiment. They will have to be confirmed in future studies with measurements acquired in other regions and geophysics conditions.

Although we investigated many parameters which influence the T_A, we are not able to fully reconcile the CAROLS radiometric noise with the root-mean-square error between measured and simulated T_A. The measurements error is lower in V-pol at moderate wind speed ($<$9 m/s) (0.15 K) than at higher wind speed or in H-pol (about 0.25 K). Hence, it could be linked to roughness influence not fully taken into account. Nevertheless, it is amongst the smallest observed error with similar instruments during other airborne campaigns.

Appendix A: RFI Detection and Mitigation Algorithm

Various methods exist to sort measured data affected by RFI. One type of method largely used for radiometric measurements [*Ruf et al*., 2006; *Skou et al*., 2010] is based on a threshold applied on the kurtosis of the antenna temperature distribution. Applied on our CAROLS raw data (kurtosis estimated on a distribution of 139.400 samples per 1 ms integration intervals), it turned out to be not fully appropriate: indeed after rejection using this criterion, high CAROLS T_A remain despite normal values of kurtosis (excess T_A up to 60 K in V and 30 K in H on 1 ms measurements). Besides, we observe that the estimated kurtosis increases slightly with the measured T_A (varying from 2.91 to 2.97 when T_A in H or V-pol varies from 70 to 240 K—not shown). Therefore, it turns out that the kurtosis is a function of polarization and incidence angle. We do not understand the origin of this variation but it could be linked to the digitization process [*De Roo and Misra*, 2008]. To avoid this issue, we propose an adaptive algorithm to filter RFI. For each block of 800 ms:

1. median calculation of T_A and k for the two polarizations;

2. standard deviation estimation using interquartile range (std_{iqr}) of $T_{A,1ms}$ and k_{1ms} for the two polarizations;

3. outlier flag for each measurements if: $|X - median(X)| > 3.std_{iqr}(X)$ for one of the four X; where X is $T_{A,1ms}$ or k_{1ms} in H or V-pol; and

4. RFI flag up when more than 2% of measurements are flagged as outlier.

Acknowledgments

The authors acknowledge Mehrez Zribi, Pascal Fanise, and Mickael Pardé for providing CAROLS measurements. The authors wish to thank the crew of the RV Côtes de la Manche as well as the technical teams from SAFIRE and DT-INSU. The authors also thank Gérard Caudal and Xiaobin Yin for very fruitful discussions, Joe Tenerelli for providing the Terrestrial Radiometry Analysis Package and Nicolas Martin for computation support. The authors thank Meteo France for providing data for the Gascogne Buoy and for providing us support during the airborne campaign. The authors also acknowledge Remote Sensing Systems for providing free and open access to SSMIS measurements. The development of the CAROLS instrument and the flight campaigns have been funded through the support of the French Space Agency CNES/TOSCA. Adrien Martin has been funded by a CNES/CNRS grant.

References

Alory, G., C. Maes, T. Delcroix, N. Reul, and S. Illig (2012), Seasonal dynamics of sea surface salinity off panama: The far eastern pacific fresh pool, *J. Geophys. Res.*, *117*, C04028, doi:10.1029/2011JC007802.

Bentamy, A., Y. Quilfen, P. Queffeulou, and A. Cavanie (1994), Calibration of the ERS-1 scatterometer C-band model, *Tech. Rep. DRO/OS-94-01*, 72 pp., IFREMER, Brest, France.

Blanch, S., and A. Aguasca (2004), Seawater dielectric permittivity model from measurements at L-band, in *Geoscience and Remote Sensing Symposium, 2004, IGARSS'04, Proceedings of the 2004 IEEE International*, vol. 2, pp. 1362–1365, IEEE Operations Center, Piscataway, N. J., doi:10.1109/IGARSS.2004.1368671.

Boutin, J., P. Waldteufel, N. Martin, G. Caudal, and E. Dinnat (2004), Surface salinity retrieved from SMOS measurements over the global ocean: Imprecisions due to sea surface roughness and temperature uncertainties, *J. Atmos. Oceanic Technol.*, *21*(9), 1432–1447, doi: 10.1175/1520-0426(2004)021<1432:SSRFSM>2.0.CO;2.

Boutin, J., N. Martin, G. Reverdin, X. Yin, and F. Gaillard (2013), Sea surface freshening inferred from SMOS and ARGO salinity: Impact of rain, *Ocean Sci.*, *9*(1), 183–192, doi:10.5194/os-9-183-2013.

Camps, A., et al. (2004), The WISE 2000 and 2001 field experiments in support of the SMOS mission: Sea surface L-band brightness temperature observations and their application to sea surface salinity retrieval, *IEEE Trans. Geosci. Remote Sens.*, *42*(4), 804–823, doi:10.1109/TGRS.2003.819444.

De Roo, R., and S. Misra (2008), A demonstration of the effects of digitization on the calculation of kurtosis for the detection of RFI in microwave radiometry, *IEEE Trans. Geosci. Remote Sens.*, *46*(10), 3129–3136, doi:10.1109/TGRS.2008.916483.

Dee, D. P., et al. (2011), The ERA-Interim reanalysis: Configuration and performance of the data assimilation system, *Q. J. R. Meteorol. Soc.*, *137*(656), 553–597, doi:10.1002/qj.828.

Dinnat, E., J. Boutin, G. Caudal, and J. Etcheto (2003), Issues concerning the sea emissivity modeling at L band for retrieving surface salinity, *Radio Sci.*, *38*(4), 8060.

Durden, S., and J. Vesecky (1985), A physical radar cross-section model for a wind-driven sea with swell, *IEEE J. Oceanic Eng.*, *10*(4), 445–451, doi:10.1109/JOE.1985.1145133.

Elfouhaily, T., B. Chapron, K. Katsaros, and D. Vandemark (1997), A unified directional spectrum for long and short wind-driven waves, *J. Geophys. Res.*, *102*(C7), 15,781–15,796, doi:10.1029/97JC00467.

Etcheto, J., E. Dinnat, J. Boutin, A. Camps, J. Miller, S. Contardo, J. Wesson, J. Font, and D. Long (2004), Wind speed effect on L-band brightness temperature inferred from EuroSTARRS and WISE 2001 field experiments, *IEEE Trans. Geosci. Remote Sens.*, *42*(10), 2206–2213.

Font, J., et al. (2012), SMOS first data analysis for sea surface salinity determination, *Int. J. Remote Sens.*, *34*(9–10), 3654–3670, doi:10.1080/01431161.2012.716541.

Gabarró, C., J. Font, A. Camps, M. Vall-llossera, and A. Julià (2004), A new empirical model of sea surface microwave emissivity for salinity remote sensing, *Geophys. Res. Lett.*, *31*, L01309, doi:10.1029/2003GL018964.

Guimbard, S. (2010), Interprétation et modélisation de mesures à distance de la surface marine dans le domaine micro-onde, PhD thesis, Université Versailles-Saint-Quentien-en-Yvelines, Versailles, France.

Guimbard, S., J. Gourrion, M. Portabella, A. Turiel, C. Gabarro, and J. Font (2012), SMOS Semi-empirical ocean forward model adjustment, *IEEE Trans. Geosci. Remote Sens.*, *50*(5), 1676–1687, doi:10.1109/TGRS.2012.2188410.

Hauser, D., G. Caudal, S. Guimbard, and A. Mouche (2008), A study of the slope probability density function of the ocean waves from radar observations, *J. Geophys. Res.*, *113*, C02006, doi:10.1029/2007JC004264.

Hernandez, O., J. Boutin, N. Kolodziejczyk, G. Reverdin, N. Martin, F. Gaillard, N. Reul, and J. Vergely (2014), SMOS salinity in the subtropical north Atlantic salinity maximum. Part I: Comparison with Aquarius and in situ salinity, *J. Geophys. Res.*, doi:10.1002/2013JC009610, in press.

Hersbach, H., A. Stoffelen, and S. de Haan (2007), An improved C-band scatterometer ocean geophysical model function: CMOD5, *J. Geophys. Res.*, *112*, C03006, doi:10.1029/2006JC003743.

IOC, SCOR, and IAPSO (2010), The international thermodynamic equation of seawater-2010: Calculation and use of thermodynamic properties, in *Manuals and Guides 56*, English ed., Intergov. Oceanogr. Comm., UNESCO, Paris.

Johnson, J., and M. Zhang (1999), Theoretical study of the small slope approximation for ocean polarimetric thermal emission, *IEEE Trans. Geosci. Remote Sens.*, *37*(5), 2305–2316, doi:10.1109/36.789627.

Klein, L., and C. Swift (1977), An improved model for the dielectric constant of sea water at microwave frequencies, *IEEE J. Oceanic Eng.*, *2*(1), 104–111.

Kudryavtsev, V., D. Hauser, G. Caudal, and B. Chapron (2003), A semiempirical model of the normalized radar cross-section of the sea surface. 1: Background model, *J. Geophys. Res.*, *108*(C3), 8054, doi:10.1029/2001JC001003.

Lagerloef, G., C. Swift, and D. M. Le Vine (1995), Sea surface salinity: The next remote sensing challenge, *Oceanography*, *8*(2), 44–50.

Lagerloef, G., F. Wentz, S. Yueh, H.-Y. Kao, G. C. Johnson, and J. M. Lyman (2012), Aquarius satellite mission provides new, detailed view of sea surface salinity, in *State of the Climate in 2011*, vol. 93, edited by J. Blunden and D. S. Arndt, chap. S70–S71, pp. S1–S282, American Meteorological Society, Boston, Mass., doi:10.1175/2012BAMSStateoftheClimate.1.

Lang, R., Y. Jin, C. Utku, S. Gu, and D. Le Vine (2010), A new model function for the permittivity of seawater at 1.413 GHz, in *2010 11th Specialist Meeting on Microwave Radiometry and Remote Sensing of the Environment (MicroRad)*, pp. 121–123, IEEE Operations Center, Piscataway, N. J., doi:10.1109/MICRORAD.2010.5559576.

Lecornu, F., and Y.-H. De Roeck (2009), Previmer-coastal observations and forecasts, *Houille Blanche*, *1*, 60–63.

Lee, T., G. Lagerloef, M. M. Gierach, H.-Y. Kao, S. Yueh, and K. Dohan (2012), Aquarius reveals salinity structure of tropical instability waves, *Geophys. Res. Lett.*, *39*, L12610, doi:10.1029/2012GL052232.

Martin, A., et al. (2012), Remote sensing of sea surface salinity from CAROLS L-band radiometer in the Gulf of Biscay, *IEEE Trans. Geosci. Remote Sens.*, *50*(5), 1703–1715, doi:10.1109/TGRS.2012.2184766.

Meissner, T., and F. Wentz (2012), The emissivity of the ocean surface between 6 and 90 GHz over a large range of wind speeds and earth incidence angles, *IEEE Trans. Geosci. Remote Sens.*, *50*(8), 3004–3026, doi:10.1109/TGRS.2011.2179662.

Mouche, A. (2005), Apport de la double polarisation pour l'étude expérimentale et théorique de la section efficace radar de la surface océanique, PhD thesis, Université Versailles Saint-Quentin-En-Yvelines, Versailles, France.

Mouche, A., D. Hauser, J.-F. Daloze, and C. Guerin (2005), Dual-polarization measurements at C-band over the ocean: Results from airborne radar observations and comparison with ENVISAT ASAR data, *IEEE Trans. Geosci. Remote Sens.*, *43*(4), 753–769, doi:10.1109/TGRS.2005.843951.

Pardé, M., M. Zribi, P. Fanise, and M. Dechambre (2011), Analysis of RFI: Issue using the CAROLS L-Band experiment, *IEEE Trans. Geosci. Remote Sens.*, *49*(3), 1063–1070, doi:10.1109/TGRS.2010.2069101.

Reul, N., J. Tenerelli, B. Chapron, S. Guimbard, V. Kerbaol, and F. Collard (2006), *CoSMOS OS Campaign*, IFREMER, Brest, France.

Reul, N., J. Tenerelli, B. Chapron, S. Guimbard, S.-S. Picard, P.-Y. Le Traon, and S. Zine (2008), Preparing the potential and challenge of remote sensing-based sea surface salinity estimation: The CoSMOS airborne campaign, in *Proceedings of the SPIE 7150*, edited by R. J. Frouin et al. p. 715006, doi:10.1117/12.804940.

Reul, N., et al. (2013), Sea surface salinity observations from space with the SMOS satellite: A new means to monitor the marine branch of the water cycle, *Surv. Geophys.*, *35*, 681–722, doi:10.1007/s10712-013-9244-0.

Rotbøll, J., S. S. Søbjærg, and N. Skou (2003), A novel L-band polarimetric radiometer featuring subharmonic sampling, *Radio Sci.*, *38*(3), 8046, doi:10.1029/2002RS002666.

Ruf, C., S. Gross, and S. Misra (2006), RFI detection and mitigation for microwave radiometry with an agile digital detector, *IEEE Trans. Geosci. Remote Sens.*, *44*(3), 694–706, doi:10.1109/TGRS.2005.861411.

Skou, N., S. Misra, J. Balling, S. Kristensen, and S. Sobjaerg (2010), L-Band RFI as experienced during airborne campaigns in preparation for SMOS, *IEEE Trans. Geosci. Remote Sens.*, *48*(3), 1398–1407.

SMOS Team (2008), SMOS L2 OS Algorithm Theoretical Baseline Document, *Tech. Rep*. SO-TN-ARG-GS-0007, ICM-CSIC, LOCEAN/LATMOS, IFREMER, ARGANS Limited, Derriford, Plymouth, Devon, U. K.

Tenerelli, J., N. Reul, A. Mouche, and B. Chapron (2008), Earth-viewing L-band radiometer sensing of sea surface scattered celestial sky radiation. Part I: General characteristics, *IEEE Trans. Geosci. Remote Sens.*, *46*(3), pp. 659–674, ARGANS Limited, Derriford, Plymouth, Devon, U. K.

Tolman, H. L. (2009), User manual and system documentation of WAVEWATCH III TM version 3.14, *Tech. Note 276*, MMAB Contrib. U. S. Department of Commerce, National Oceanic and Atmospheric Administration, Camp Springs, Md.

Yin, X., J. Boutin, N. Martin, and P. Spurgeon (2012), Optimization of L-band sea surface emissivity models deduced from SMOS data, *IEEE Trans. Geosci. Remote Sens.*, *50*(5), 1414–1426, doi:10.1109/TGRS.2012.2184547.

Yueh, S. (1997), Modeling of wind direction signals in polarimetric sea surface brightness temperatures, *IEEE Trans. Geosci. Remote Sens.*, *35*(6), 1400–1418, doi:10.1109/36.649793.

Yueh, S., S. Dinardo, A. Fore, and F. Li (2010), Passive and active L-band microwave observations and modeling of ocean surface winds, *IEEE Trans. Geosci. Remote Sens.*, *48*(8), 3087–3100, doi:10.1109/TGRS.2010.2045002.

Yueh, S., W. Tang, A. Fore, G. Neumann, A. Hayashi, A. Freedman, J. Chaubell, and G. Lagerloef (2013), L-Band passive and active microwave geophysical model functions of ocean surface winds and applications to Aquarius retrieval, *IEEE Trans. Geosci. Remote Sens.*, *51*(9), 4619–4632, doi:10.1109/TGRS.2013.2266915.

Zribi, M., et al. (2011), CAROLS: A new airborne L-band radiometer for ocean surface and land observations, *Sensors*, *11*, 719–742.